

# Internal current collection and thermofluidynamic enhancement in a microtubular SOFC

Hodjati-Pugh, Oujen; Dhir, Aman; Steinberger-Wilckens, Robert

DOI:

[10.1016/j.ijheatmasstransfer.2021.121255](https://doi.org/10.1016/j.ijheatmasstransfer.2021.121255)

License:

Creative Commons: Attribution-NonCommercial-NoDerivs (CC BY-NC-ND)

*Document Version*

Peer reviewed version

*Citation for published version (Harvard):*

Hodjati-Pugh, O, Dhir, A & Steinberger-Wilckens, R 2021, 'Internal current collection and thermofluidynamic enhancement in a microtubular SOFC', *International Journal of Heat and Mass Transfer*, vol. 173, 121255. <https://doi.org/10.1016/j.ijheatmasstransfer.2021.121255>

[Link to publication on Research at Birmingham portal](#)

## General rights

Unless a licence is specified above, all rights (including copyright and moral rights) in this document are retained by the authors and/or the copyright holders. The express permission of the copyright holder must be obtained for any use of this material other than for purposes permitted by law.

- Users may freely distribute the URL that is used to identify this publication.
- Users may download and/or print one copy of the publication from the University of Birmingham research portal for the purpose of private study or non-commercial research.
- User may use extracts from the document in line with the concept of 'fair dealing' under the Copyright, Designs and Patents Act 1988 (?)
- Users may not further distribute the material nor use it for the purposes of commercial gain.

Where a licence is displayed above, please note the terms and conditions of the licence govern your use of this document.

When citing, please reference the published version.

## Take down policy

While the University of Birmingham exercises care and attention in making items available there are rare occasions when an item has been uploaded in error or has been deemed to be commercially or otherwise sensitive.

If you believe that this is the case for this document, please contact [UBIRA@lists.bham.ac.uk](mailto:UBIRA@lists.bham.ac.uk) providing details and we will remove access to the work immediately and investigate.

# Internal current collection and thermofluidynamic enhancement in a microtubular SOFC

O. Hodjati-Pugh<sup>a</sup>, A. Dhir<sup>b</sup>, R. Steinberger-Wilckens<sup>a</sup>

<sup>a</sup>Centre for Fuel Cell and Hydrogen Research,

School of Chemical Engineering, University of Birmingham, B15 2TT

<sup>b</sup>School of Chemical Engineering, University of Wolverhampton, WV1 1LY

## Abstract

A low-cost, durable and simple internal current collector is presented for microtubular SOFCs ( $\mu$ T-SOFC). The internal design does not require removal of external cell layers, and subsequent loss of active area required to expose the interior electrode for contacting. The brush-like, high surface area current collector device is adapted from heat exchanger turbuliser technology produced by CALGAVIN Ltd. The effectiveness of the hiTRAN<sup>®</sup> turbuliser as a  $\mu$ T-SOFC current collector is explored and its thermofluidynamic effects on the cell described, as well as coating of the hiTRAN<sup>®</sup> design to reduce electrical contact resistance. The final design achieved a current density at 0.7 V of  $0.38 \text{ A.cm}^{-2}$  and peak power density of  $0.27 \text{ W.cm}^{-2}$ , 4.3 times higher than the original design and 3.3 times higher than the state-of-the-art with the same base materials.

**Keywords:** Tubular SOFC, current collection, internal current collector, interconnection, pseudo turbulence, thermofluidynamics

## 1.0 Introduction

Solid oxide fuel cells are highly efficient electrochemical conversion devices with electrical efficiency of 55 to 60% and combined heat and power efficiency (CHP) of up to 85% [1]. Fuel cells are zero-emission power devices provided they are fed with 'green' fuels from renewables or with biogas. Tubular solid oxide fuel cells have inherently favourable characteristics over their more common planar counterparts, namely rapid start-up times, high thermo-mechanical durability, and high stack power density [2,3]. The aforementioned widen the market opportunities for SOFCs to include portable applications, typically currently reserved for low-temperature fuel cells [4,5].

A long-established bottleneck of tubular fuel cells are long electron conduction pathways leading to elevated ohmic polarisation, restricting the cell design, particularly cell length [6,7]. Increasing the number of current collectors in a given cell length reduces the conduction length, but is typically achieved at the expense of active area, reducing the total power output potential of a cell

[8]. Accessing the inner electrode of a tubular cell is particularly difficult. The inner electrode, the anode in an anode supported cell, can be accessed from the cell exterior or the cell interior [9]. The state-of-the-art is an external anode current collector located at the centre of the active region [10,11]. This typically requires removal of exterior layers to expose the anode interior. Doing so weakens the cell support leading to higher risk of mechanical failure, as well as creating an additional requirement for sealing, another key area of development in SOFC technology [12,13]. Failure to provide a durable hermetic seal can lead to fuel crossover and combustion, lowering conversion efficiency and accelerating degradation due to local thermal hot-spots [14,15].

Internal current collection in tubular cells has been used in many forms such as meshes, foams and coils inserted into the tube bore. Internal current collectors do not require cutting of external cell layers, maximising the available active area, alleviating the associated mechanical and durability limitations of the external design [16–18]. Furthermore, internal current collectors can contact a large area of the electrode and be spaced along the cell length, reducing the current conduction pathway length to reduce the cell area specific resistance (ASR) [19]. However, the internal design comes with its own limitations. Ensuring a sufficient contact area and contact force/pressure between the internal current collector and the electrode throughout the cell operation lifetime is imperative to minimise contact resistance and its effect on the cell ASR [20,21]. The small diameter of  $\mu$ T-SOFCs makes access difficult and the use of joining or contact pastes difficult. For tubes with a diameter of less than 2 mm, researchers have typically relied on the elasticity of the current collector material (mostly metals) to maintain contact with the electrode wall. However, loss of contact is commonly reported for small diameter designs, the effect being even more severe for larger diameter  $\mu$ T-SOFCs [22]. This loss of contact leads to a low cell performance from a high ohmic polarisation.

Internal current collectors also affect the flow within a tubular cell, which is the fuel side for an anode supported cell. Care must be taken not to impede the fuel flow within the tube channel and avoid blockage of the porous anode walls [23]. However, the internal current collector can be used to enhance the fluid dynamics and mass transport to increase the conversion of fuel into electricity and improve heat transfer [24]. Research by Rahimi et al. showed a 41% increase in performance of a polymer electrolyte fuel cell (PEFC) when using a coil insert in the flow channels compared to the empty channel. The increase in performance was ascribed to the increased radial velocity and better mixing in the modified flow dynamics caused by the insert [25].

In this context, the design of an internal current collector with a high surface area, short conduction pathway length and a good current collector-electrode contact was explored in this study via electrical, electrochemical and mechanical testing. Materials development and coatings

were explored to reduce contact resistance. The effect of the current collector design variables, namely packing density, on the thermofluidynamics was explored using measurement of pressure drop and temperature. The latter was captured via thermal imaging, infra-red thermometry and thermocouples, measuring both surface and fluid temperature.

## 2.0 Experimental

### 2.1 Electrochemical Characterisation of $\mu$ T-SOFCs

The  $\mu$ T-SOFC cells and cell testing setup can be seen in [9] (described previously) and in Supplementary Material Section (SM) 3.0. A single central external current collector was included in some cell test setups for comparative analysis to the state-of-the-art current collector configuration. The anode supported cells were 152 mm in length, with an outer diameter of 6.8 mm, cathode length of 95.5 mm and an active area of 20 cm<sup>2</sup>. The anode was Ni-YSZ, the electrolyte YSZ, the barrier layer GDC, and the cathode LSCF. Polarisation and power density plots and electrochemical impedance spectroscopy (EIS) data was acquired using a Solartron Analytical 1470E Cell Test System coupled to a Solartron ESIS unit and data logger.

### 2.2 Turbuliser Implementation for Electrochemical Testing

The fitting direction of the brush-like hiTRAN<sup>®</sup> turbuliser, as seen in Figure 1, was from right to left in the case shown (opposite to the fuel flow direction) leading the tail through the outlet region of the cell. An introduction to the hiTRAN<sup>®</sup> technology can be seen in SM Section 1.1. Three turbuliser designs were trialled, varying coil packing density from low (LPD) to medium (MPD) and high (HPD). Varying packing density affects the thermofluidynamics but here was varied to adjust the current collector contact area with the anode wall. More details on the turbuliser design and specifications can be seen in SM Section 2. All turbulisers had a central support core wire with a 1.42 mm outer diameter (OD) and 250 mm length, a 100 mm of which was threaded with a coil section to contact the entire 95.5 mm cathode. The core acted as a current 'highway', extracting the current collected (0.375 mm OD) by the coils at the anode interior wall. Once 70 mm of the 100 mm loop section were inside the cell, the spring force of the coils of the oversized turbuliser coil against the cell wall provided a strong resistance to motion. It was found that a steady and continuous feed speed was the key to minimise damage to the turbuliser and the cell.

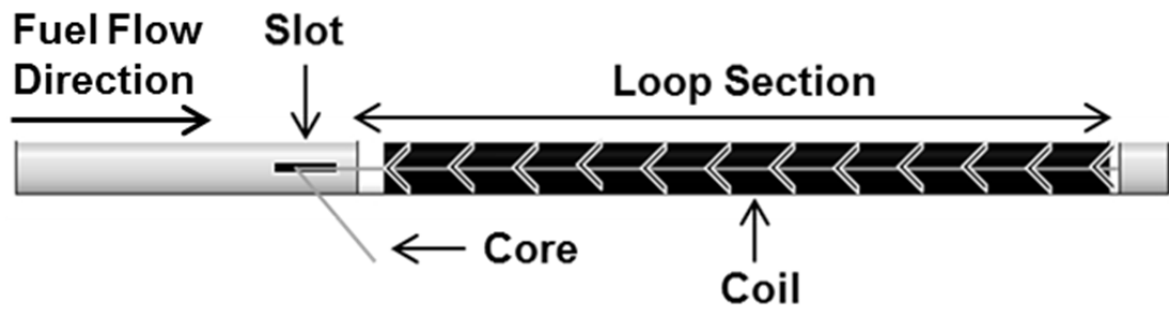


Figure 1 - Installing a hiTRAN® turbuliser inside a  $\mu$ T-SOFC [9].

A slot was required to allow the remaining core wire of the turbuliser to exit the cell for connection to the external circuit and/or for interconnection. This avoided manifold complexity and reduced the interconnection path length, minimising ohmic losses.

To cut these slots, a Lasea Multi-Axis Laser with a stack of 5 mechanical stages, 3 linear and 2 rotary axes, and a 3D scan head with 3 optical axes was used. The laser had a cold beam which prevented damage to fuel cell components from thermal hot spots. The laser featured a controllable cutting depth. This allowed a single window to be made on one side of the cell, leaving less area to subsequently seal, avoiding gas leakages. Details of the laser and slot development are seen in SM 4.0.

The installed turbuliser within the cell and the inlet manifold design is seen in Figure 2. Two alumina tubes were used for the inlet manifold. A small bore fuel inlet supply tube and a larger bore inlet support tube. The inlet support tube covered the sealed slot (details of which are found in [9]) to provide additional mechanical sealing to minimise leakage. The inlet supply tube protruded past the slot and the inlet support tube, further minimising the potential for leakage, ejecting fuel into the  $\mu$ T-SOFC directly prior to the active region (indicated by the black area in Figure 2).

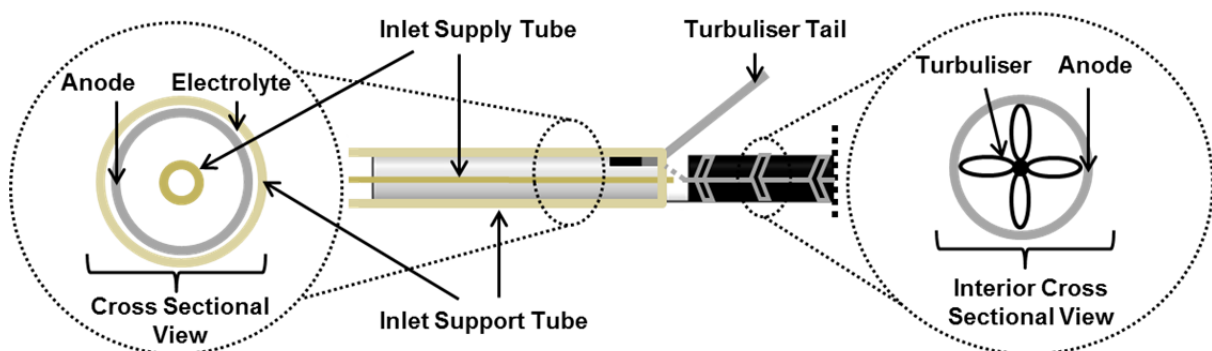


Figure 2 - Inlet  $\mu$ T-SOFC cross-section with turbuliser, with a zoom-in on the inlet manifold and the cell interior with turbuliser.

## 2.3 Turbuliser Thermofluidynamic Testing

The hiTRAN® turbuliser removes the laminar boundary layer by inducing turbulence (pseudo/quasi-turbulence) in the tube side fluid, thereby reducing the thickness of the velocity and thermal boundary layer and therefore reducing the resistance to heat transfer and mass transfer [26]. The turbuliser promotes better mixing, ensuring fresh fuel is supplied to the electrode from the free stream thereby reducing mass transport losses. Further information on the turbuliser thermofluidynamic mechanisms and flow regime in  $\mu$ T-SOFCs can be seen in SM Section 1.2. The pressure drop across the fuel cell was measured using a Digitron digital differential pressure meter with a 0 to 250 Pa measurement range. The pressure drop was calculated across anode inlet and outlet manifold, giving insight into the flow characteristics and residence time within the cell. The pressure measurement was conducted in parallel with the flow and had a negligible effect on the flow. A quartz tube with similar internal diameter to the fuel cell was also used for pressure measurement using the same differential pressure meter. The quartz tube was used as a simple way of measuring the flow effects of the turbuliser, avoiding the lengthy setup of a real fuel cell while also mitigating the risk of potential leakage from fuel cell-manifold/current collector joints, and loss of valuable micro-tubes.

To investigate the heat transfer impact of the turbuliser, the temperature of the fuel and fuel cell were measured with and without the turbuliser installed using the same cell setup as for electrochemical testing, again using the quartz tube setup as a simulated fuel cell. CALGAVIN Ltd. states that broadly speaking, the hiTRAN® turbuliser will give a 2 to 4 fold improvement in the heat transfer coefficient. While this was not a primary objective of the study, understanding the thermal effects of the turbuliser was important for developing more insight into the sensitivities of cell performance.

Accurate measurement of temperature at typical SOFC operating conditions is non-trivial. Three temperature measurement techniques were used in this study to get as complete an understanding as possible, namely thermal imaging, and infra-red and thermocouple thermometry. Thermal imaging and the infra-red thermometry could be done from outside the hot zone of the furnace and were non-invasive techniques to measure surface temperatures. They operate by detecting radiation absorbed/emitted by a body and require knowledge of the emissivity of the sample being analysed. Thermocouples use the thermoelectric effect and thus must be placed inside the furnace. Placement of the thermocouple is crucial to ensure the correct temperature is being measured. Thermocouples can be used to measure surface temperature and fluid temperature. Contacting of the fuel cell components would be invasive and could lead to short-circuiting given the metallic surface of the thermocouple. Consideration had also to be given to account for the inertia in

changes in measurement values from a thermocouple. The thermocouple tip was insulated with a white ceramic insulator tip to maintain a steady probe temperature, shielded from radiation.

## 2.4 Mechanical Testing

Mechanical testing of the current collector-anode joints was conducted using an Instron 5848 Environmental Mechanical Tester (Instron). The Instron had a fixed lower vice grip and an upper vice grip attached to a 100 N load cell. To avoid any damage to the fuel cell when securing in the vice grip, the fuel cell was loaded into an in-house fabricated metal cell holder which would then be held in the vice. The tubular cell holder was 180 mm in length, had an 8 mm outer diameter with a flat stop at the end which only the current collector wire could pass through to be held in the vice grip of the upper load cell. The Instron was controlled using Bluehill software which was used to set the extension rate, to 2 mm per minute with a maximum extension of 20 mm.

## 3.0 Results and Discussion

### 3.1 Fluid Dynamics

The pressure drop across a quartz tube with the same internal diameter as the fuel cell and a similar length was used to measure the pressure drop across the  $\mu$ T-SOFC. Measurements were made at 25°C instead of at SOFC operating conditions to avoid the rapid volume change of the gas, and thus the acceleration that would occur from heating. Measurements were then compared to an estimated pressure drop,  $\Delta P$  [Pa] using the Darcy-Weisbach equation (1) [27].

$$\Delta P = f_D * \frac{L}{D} * \frac{\rho v^2}{2} \quad (1)$$

Where  $L$  [m] is the tube length,  $D$  [m] the tube diameter,  $\rho$  [kg.m<sup>-3</sup>] the fluid viscosity and  $v$  the fluid velocity [m.s<sup>-1</sup>]. The Darcy friction factor,  $f$  [-], for laminar flow in a pipe (empty tube) is given by (2):

$$f_D = \frac{64}{Re} \quad (2)$$

Friction factor correlations as seen in (3) were provided by CALGAVIN Ltd as a function of packing density, Reynolds number and design parameters ( $\alpha, \beta$ ) which were estimated for each hiTRAN® turbuliser design and substituted into (1):

$$turbuliser f_D = f(PD, \alpha, Re^{-\beta}) \quad (3)$$

A baseline empty-tube measurement was used to show improvement, in an analogy to the tubular SOFC with external current collection only. Measurements were made at the fuel cell testing fuel flow conditions of 200 ml.min<sup>-1</sup> of H<sub>2</sub>. The estimated friction factor, estimated pressure drop and percentage increase in pressure drop versus an empty tube are seen in Table 1. For these conditions,

the Reynolds number was very low at 7.2, indicating laminar flow conditions, far from any transition to turbulent conditions ( $Re = 2300$ ) [28].

**Table 1 - Varying hiTRAN® PD vs friction factor and pressure drop.**

	Empty tube	LPD	MPD	HPD
<b>Friction Factor [-]</b>	30.3	41.9	61.6	121.3
<b>Pressure Drop [Pa]</b>	0.7	1.0	1.4	2.8
<b>Increase from Base [%]</b>	-	42	100	300

**Place Figure 3 here**

**Figure 3 - Measured and estimated pressure drop of empty tube versus LPD, MPD and HPD turbuliser.**

The estimated pressure drop and measured pressure drop are plotted in **Error! Reference source not found.** for the empty tube and the LPD, MPD and HPD turbulisers. The empty tube and LPD pressure drop as recorded was under-predicted in comparison to the estimated, while the MPD and HPD configurations over-predicted the pressure drop, with the MPD showing the best fit. It was seen that increasing the packing density increased the pressure drop as expected. It should be noted that the correlations for friction factor provided by CALGAVIN Ltd were from experimental data using 10 mm ID and above. Using extrapolation of the data, correlations were provided for the 5.5 mm ID of the fuel cell. The standard deviation for all measurements was below  $\pm 0.06$  Pa. A 42%, 100% and 300% increase over the base case empty tube was recorded for the LPD, MPD and HPD



turbulisers, respectively. A 40% increase in pressure drop was measured between the LPD and MPD, and a 100% increase between the MPD and HPD turbulisers. A lower pressure drop was considered more favourable for reducing parasitic pumping loss of blowers which would be multiplied by the number of cells across a stack; hence the LPD and MPD were the favoured designs. However, operating the cell with a higher back pressure would increase the Nernst potential and increase fuel cell efficiency at a given current density which would again favour the HPD turbuliser as seen from (4).  $R$  is the universal gas constant ( $\text{J.mol}^{-1}.\text{K}^{-1}$ ),  $F$  is Faradays constant,  $T$  (K) is the temperature and  $P$  is the pressure (Pa).

$$\Delta V = \frac{RT}{4F} \ln \left( \frac{P_2}{P_1} \right) \quad (4)$$

### 3.2 Heat Transfer

The thermal image of the inlet region of the tubular cell with a central current collector and MPD turbuliser overlaid with a labelled schematic is seen in Figure 4. The reference bar is in °C and the scale has increments of 60°C. The fuel cell was tested at the standard operating conditions of 750°C and a 200 ml.min<sup>-1</sup> H<sub>2</sub> fuel flow. The image gives information on the surface temperature of the cell setup. It was seen that the fuel entering at 25°C was rapidly heated in the inlet manifold as per the transition from purple to a dark orange but did not reach the peak temperature of 748°C at the beginning of the active area. The white, hottest region was at the cell centre. The wire and insulation leaving the central current collector are blocking some of the image.

The infra-red thermometer was used on the same cell to confirm the surface temperature measured by the thermal imaging camera. Values were recorded at start, centre and end of the active region. **Error! Reference source not found..** The average temperature at the inlet region was 742°C, at the central current collector was 748°C and at the outlet region was 747°C. The error values were ±1.7°C, ±2.6°C and ±2°C, respectively. This confirmed that there was a temperature profile along the active region. The inlet region was cooled by the fuel entering at room temperature. At the operating potential of 0.7 V, the cell produced heat through exothermic electrochemical reactions and through ohmic heating. The central node through which current was drawn was the hottest region and the temperature tended towards the furnace temperature. At the outlet region, the fuel that had travelled through the hot zone became hotter than at the inlet region. At the outlet region, there was less fuel to provide cooling and hence the temperature was on average 1°C below the central node and around 5°C hotter than at the inlet. As the fuel heated up and tended towards the furnace temperature, the driving force for heat transfer was reduced. The image can be considered to be at a steady-state where thermal equilibrium has been achieved.

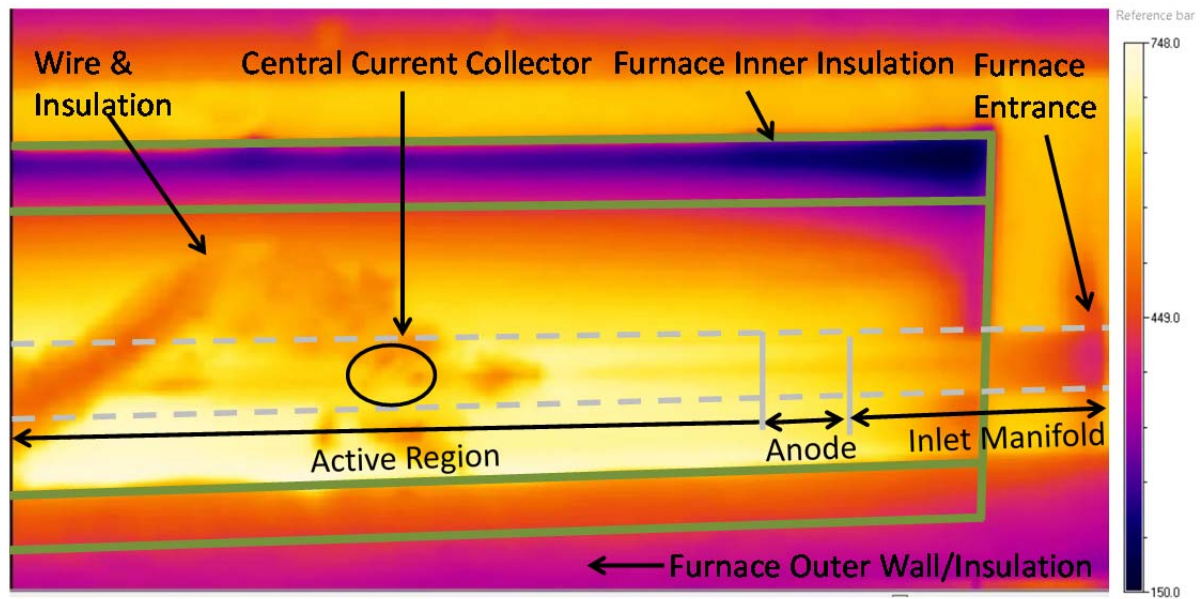
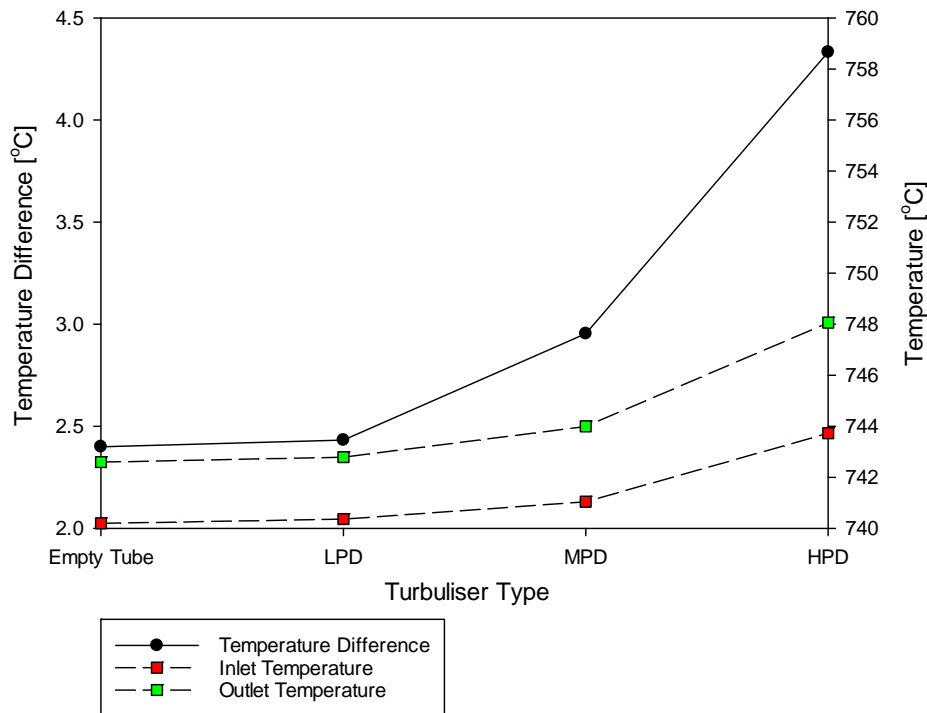


Figure 4 - Thermal image of a cell with central current collection and MPD hiTRAN® in the furnace at 0.7 V at the standard operating conditions of 750°C and a flow of 200 ml.min<sup>-1</sup> H<sub>2</sub> and 10 ml.min<sup>-1</sup> N<sub>2</sub>.

To remove any temperature effects from fuel combustion (arising from leakages associated with real-world testing of a cell) and to obtain a measurement of the fuel temperature rather than fuel cell surface temperature, the quartz tube setup was used again. The thermocouples were placed 2 mm before and 2 mm after the turbuliser loop section in the free stream within the quartz tube. This was to simulate the fluid temperatures that would be observed just prior and after the active region of the cell where the turbuliser loop sections would sit. The values would represent the fuel cell at OCV when there is no heat generation. The temperatures were measured at the same location for the empty tube and for the LPD, MPD and HPD turbuliser. Care was taken to ensure the thermocouple tip did not touch the wall of the tube or the turbuliser. The inlet and outlet temperatures and the temperature difference are seen in Figure 5. The average temperature difference was 2.4°C for the empty tube, increasing marginally to 2.43°C for the LPD turbuliser. The average MPD and HPD temperature difference were 3.0°C and 4.3°C. The temperature difference error was  $\pm 0.1^\circ\text{C}$  for the empty tube and less than  $\pm 0.06^\circ\text{C}$  for the turbuliser setup. Increasing the packing density of the turbuliser acted to increase the fluid temperature difference along the cell. The turbuliser was effective at mixing the fluid and removing the laminar boundary layer, ensuring cooler fuel from the free stream, typically at the tube centre, was brought into contact with the relatively hotter tube wall which in turn absorbed heat from the furnace. The direction of the heat transfer was from the furnace air to the fuel stream. The outlet temperature increased for all turbulisers compared to the empty tube, increasing by 5.5°C to 748°C for the HPD turbuliser. Inlet temperatures also increased with the MPD and HPD turbuliser. This was somewhat unexpected but can be seen as a result of two effects. Firstly, the flow rate of the fluid decreased as the packing

density increased. This was due to the momentum loss caused by the fluid being disturbed by the fluid before the turbuliser which resulted in a pressure drop. The slower fluid velocity resulted in the fluid before the turbuliser spending longer in the pre-heating section and thus absorbing more heat, resulting in a higher temperature. Secondly, the intimate contact with the turbuliser and the wall resulted in better conductive heat transfer along the tube. This could result in an elevated wall temperature prior to the turbuliser region which would, in turn, mean a higher heat transfer rate to the fluid.



**Figure 5 - Inlet temperature, outlet temperature and temperature gradient across the turbuliser loop section position in a quartz tube at a furnace temperature of 750°C and with a 200 ml.min<sup>-1</sup> H<sub>2</sub> flow.**

Both the conductive and convective effect of the turbuliser heat transfer enhancement can be seen from Figure 6, where the inlet flow rate of hydrogen to the quartz tube was increased from zero to 400 ml.min<sup>-1</sup> for the empty tube, MPD and HPD turbuliser setup. At a flow rate of zero, the temperature difference along the cell was higher when a turbuliser was used and increased with packing density. This was explained by the increased heat conduction effects (in the axial direction) arising from the metallic and highly thermally conductive turbuliser contacting the tube wall. For the no-flow case, the inlet temperatures for the empty tube and MPD turbuliser were similar, while an increase of 4°C was observed for the HPD design. As flow was introduced and increased, the inlet temperature reduced slightly, given the larger mass of cold air entering the tube. The outlet temperature, though, remained similar. In laminar flow, doubling the flow rate will typically achieve a 10 to 20% increase in the heat transfer rate [29].

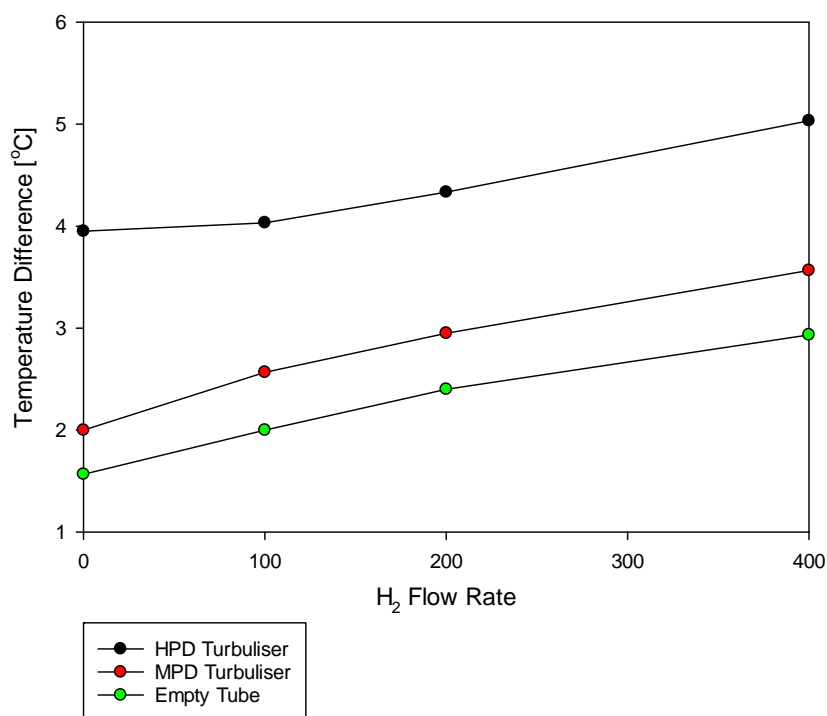


**Figure 6 - Temperature difference across the turbuliser loop section position in a quartz tube for an empty tube, MPD and HPD turbuliser versus flow rate.**

The effect of operating potential on the fuel outlet temperature was studied using a single thermocouple. It was not possible to locate a probe at the inlet without a high risk of leakage due to the manifold configuration. The outlet temperature at OCV, 0.7 V and 0.5 V for the fuel cell with a MPD turbuliser, extracting current solely using the central current collector along with the percentage increase in outlet temperature versus OCV is seen in Figure 7. As the operating potential increased, more current was produced, resulting in more heat from electrochemical reactions and ohmic losses. This caused the cell temperature to increase, which in turn heated the reactants and products exiting the cell. The outlet temperature increased from the temperature at OCV by around 0.7% and 1.8% at 0.7 V and 0.5 V, respectively. The outlet temperature of the fuel cell with MPD turbuliser and 200 ml.min<sup>-1</sup> of H<sub>2</sub> fuel flow at OCV was just below 742°C, 2°C lower than the outlet temperature from the quartz tube experiment set up at the same conditions. This small difference can be attributed to the difference of thermal conductivity of the quartz versus the ceramic manifolds and fuel cell components (primarily the Ni-YSZ), the difference in emissivity of the materials and the resulting different radiative heat transfer, and the slight difference in pressure drop between the quartz tube fittings and the more complex fuel cell setup.

place Figure 7 here

**Figure 7 - Outlet temperature from the fuel cell with MPD turbuliser at OCV, 0.7 V, 0.5 V and percentage increase in outlet temperature versus OCV.**

When used in a real-world  $\mu$ T-SOFC stack, the thermal effects of the turbuliser will be exaggerated compared to the controlled laboratory heating setup in this study. Here, the large and well-insulated furnace provides very stable heating, delivering heat by convection and radiation. In a real stack, heating is typically provided by convection only via pre-heated air from a blower directed onto the cells' exterior. Pre-heating of the fuel is also typical [5]. For portable  $\mu$ T-SOFC devices, the space for thermal lagging can be limited resulting in a large amount of heat rejection to the environment negatively impacting the thermal efficiency [4]. The turbuliser improves the heat transfer from the pre-heated fluids to the cell, reducing the heat input required to reach a desired operating temperature. This contributes to increasing system thermal efficiency and allowing for smaller pumps/blowers favouring system volumetric and gravimetric power density. The improved thermofluidynamics of a stack including turbuliser will reduce the time required to reach the desired operating temperature, further improving the start-up time and thus increasing the competitiveness of  $\mu$ T-SOFC over alternate power systems.

### **3.3 Interim Conclusions: Selecting an Optimal Design**

From a thermomechanical perspective, the LPD turbuliser would be favoured due to the relatively lower temperature gradient along the cell, 21% and 75% lower than the MPD and HPD designs, respectively. Lower temperature gradients along the cell would result in a smaller cell displacement in both the axial and radial direction, resulting in minimal stress on the manifolds, joints and sealing.

From a mass transfer perspective, the HPD would be favoured as higher heat transfer also relates to a higher mass transfer rate from the free stream into the anode, reducing mass transport losses. However, if the cell is at a higher temperature, the Nernst potential will be reduced. Nevertheless, cell efficiency increases with increasing temperature. From a pressure drop perspective, the LPD design would be favoured, with the pressure drop of the MPD and HPD being 1.4 and 2.8 times higher than the LPD, respectively. From a system weight and cost perspective, the LPD turbuliser design would be favoured. Using less material resulted in an LPD mass 5.7% and 51% lower than the MPD and HPD designs, respectively. From a resistance perspective, the LPD turbuliser would be favoured, with a resistance 7.1% and 13.7% lower than the MPD and HPD designs, respectively. However, the lower loop density would result in fewer contact points between the turbuliser and cell wall and thus a lower contact area, contact force and higher ASR. From a manufacturing perspective, the poor reproducibility and structural integrity of the LPD design favoured the MPD and HPD designs. The tradeoff in the aforementioned factors made selection difficult and so all designs were put forwards for initial testing to determine the effectiveness of the hiTRAN® designs as a current collector in a real cell. The final design could be chosen for optimisation.

### **3.4 Electrochemical Testing**

The LPD, MPD and HPD turbuliser designs were tested in three cells at the standard operating conditions of 750°C and a fuel flow of 200 ml.min<sup>-1</sup> H<sub>2</sub> and 10 ml.min<sup>-1</sup> of N<sub>2</sub>. The addition of nitrogen was chosen for the purpose of using gas chromatography (the data for which is not presented in this study) and had negligible flow, thermal or electrochemical impact. With respect to the ohmic resistance, the high frequency intercept value was extracted from raw EIS data at 0.7 V, showing that the LPD turbuliser had the highest value at 0.27 Ω. The corresponding value for the MPD and HPD turbuliser were both 0.23 Ω to 2 d.p. The relatively lower loop density of the LPD turbuliser brush meant that there were fewer contact points between the brush and the cell wall compared to the MPD and HPD designs. The lower contact area brought an increase in contact resistance. A lower number of contact points also meant that there was a weaker contact pressure between the brush and the cell wall. This was evident during the installation of the MPD and HPD brushes which required greater force to install in the tube, whereby the higher contact force between the turbuliser and the wall acted to decrease the contact resistance. The higher bulk resistance of the HPD versus the MPD design acted against this benefit and the effect of greater contact area and contact force compensated so the same resistance values were recorded. The ASR of the cells with the MPD and HPD turbulisers as the sole current collector was 5.3 Ω.cm<sup>2</sup>, indicating further optimisation was required to reduce this to an acceptable value.

The typical polarisation and power density plots of three  $\mu$ T-SOFCs with the turbulisers shown in **Error! Reference source not found.** can be seen in Figure 8. The current density achieved with the LPD turbuliser at 0.7 V was 0.075 A.cm<sup>-2</sup> and 0.081 A.cm<sup>-2</sup> for both the MPD and HPD variants. The peak power density of the LPD, MPD and HPD designs was 0.056 A.cm<sup>-2</sup>, 0.061 A.cm<sup>-2</sup> and 0.062 A.cm<sup>-2</sup>, respectively. As also indicated by the impedance analysis, the performance of the MPD and HPD turbulisers were very similar. The LPD turbuliser performed relatively poorly with the peak power density around 10% lower than the MPD and HPD designs. The ASR values estimated from the gradient of the i-V curve between 0.9 and 0.65 V were 5.6  $\Omega$ .cm<sup>2</sup>, 5.0  $\Omega$ .cm<sup>2</sup>, 4.9  $\Omega$ .cm<sup>2</sup> for the LPD, respectively. The estimate for the ASR from EIS and by the gradient of the i-V curve differed by 0.3  $\Omega$ .cm<sup>2</sup> for both the MPD and HPD turbulisers.

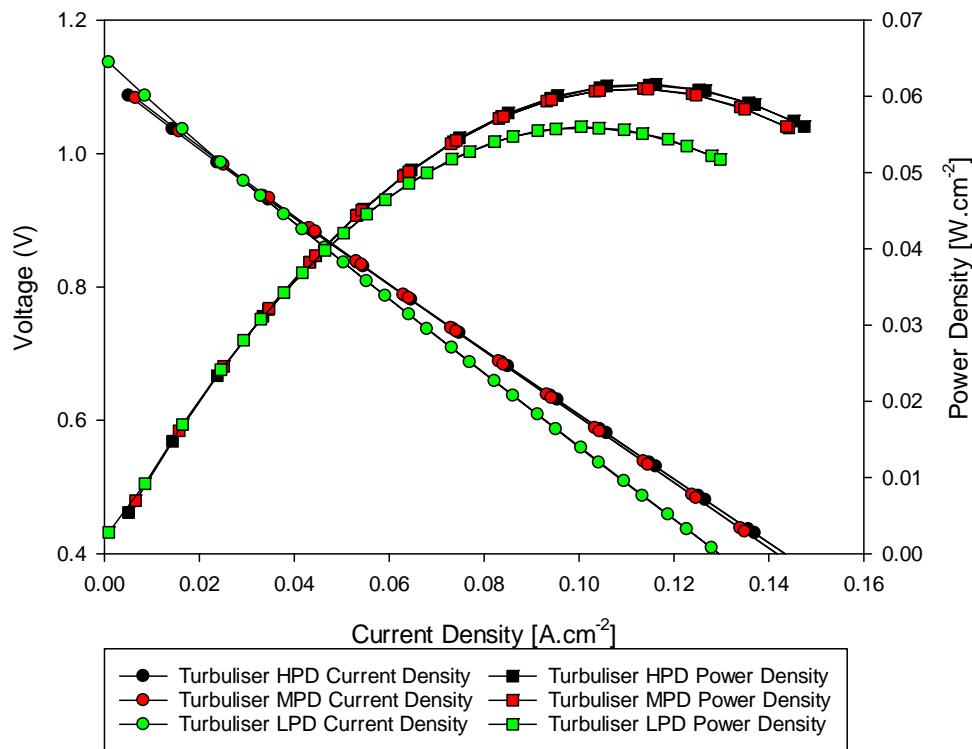


Figure 8 - Polarisation and power density plot as a function of turbuliser packing density.

### 3.5 Determining the Optimum Design

After the design, fabrication, characterisation and initial electrochemical testing had been completed it was decided to choose the MPD design for further optimisation. This decision was based on the following considerations:

- From a fabrication viewpoint, the LPD design proved difficult to manufacture consistently as the loop patterns were irregular and not secured well to the central core.

- From an installation viewpoint, the LPD design did not sit firmly in the cell compared to the MPD and HPD designs. While a firm fit was desired, the HPD design required excessive force to install and in some instances damaged the anode when pulling the tail through the laser slot. The MPD had a snug fit and became tight when all of the loop section was positioned.
- From a mass perspective, the relatively lighter LPD and MPD designs would result in a cell with a higher power density by mass which would multiply on a stack level.
- From a bulk resistance viewpoint, the LPD and MPD designs would have been favoured over the HPD design which had a higher resistance.
- From a fluid dynamics viewpoint, the lower pressure drop of the LPD turbuliser would favour lower parasitic fuel transport losses in the balance of plant, however, the higher fuel back pressure of the HPD would lead to a higher Nernst potential and thus higher efficiency. The approximately doubling of loops in a given length from the LPD to MPD design, and thus doubling of electrical contact points, on the other hand, resulted in a 12.9% increase in pressure drop
- From a heat transfer viewpoint, increasing the packing density acted to increase the temperature gradient along the cell, leading to thermomechanically induced dilation of the cell which would induce stress on the manifolds and sealing. The temperature difference in the HPD design was increased by 44% over the empty quartz tube, whereas with the MPD it was increased by 20%.

From initial EIS and polarisation data it was determined that the MPD and HPD performed similarly. The ASR of the LPD design was 11% higher than that of the MPD design. The trade-off of the aforementioned conclusions led to the selection of the MPD turbuliser design for further study and optimisation. The chosen turbuliser design was now compared against the state-of-the-art current collector design, namely the central anode current collector [30]. The combined central current collector and turbuliser current collector configuration was previously described in [9] and is seen in **Error! Reference source not found.**. The central current collector was prepared in both nickel and silver to compare the effect of the different current collector configuration and material types.

As seen in Figure 9, the current density at 0.7 V for the MPD turbuliser was  $0.08 \text{ A.cm}^{-2}$ , for the central nickel connection  $0.14 \text{ A.cm}^{-2}$ , and  $0.22 \text{ A.cm}^{-2}$  for the central silver current collector. The peak power density with the MPD turbuliser was  $0.06 \text{ W.cm}^{-2}$ , for the central nickel contact  $0.08 \text{ W.cm}^{-2}$ , and  $0.17 \text{ W.cm}^{-2}$  for the central silver current collector. The ASR estimated from the gradient of the polarisation plot for the MPD turbuliser was  $5.0 \text{ } \Omega.\text{cm}^2$ , was  $3.9 \text{ } \Omega.\text{cm}^2$  for the central



nickel connection, and  $1.7 \Omega \cdot \text{cm}^2$  for the central silver current collector. Comparing the central node connection in both silver and nickel it was evident that the effect of current collector material was a significant.

place Figure 9 here

Figure 9 - Polarisation and power density plots of turbuliser MPD, central nickel and central silver current collector.

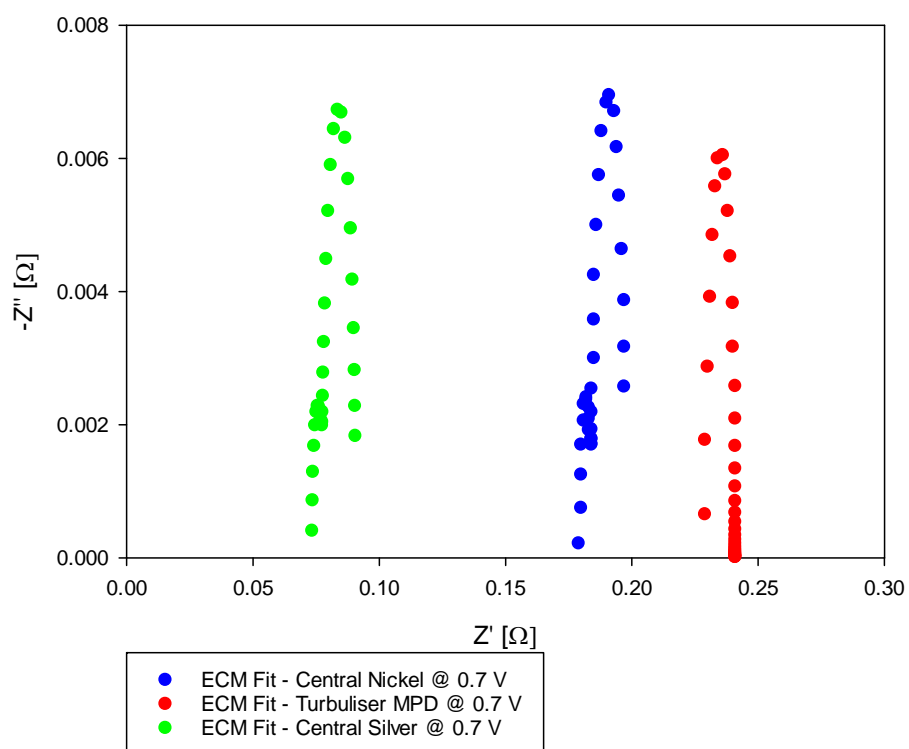


**Figure 10 - ECM impedance fit of central nickel, MPD turbuliser and central silver current collection at 0.7 V.**

From **Error! Reference source not found.**, the ohmic resistance of the MPD turbuliser, central nickel and central silver current collector was 0.234  $\Omega$ , 0.180  $\Omega$ , and 0.073  $\Omega$ , respectively. Using an active area of 19.6 mm<sup>2</sup> and the total resistance values, the ASR of the MPD turbuliser, central nickel and central silver contacting were 4.7  $\Omega\cdot\text{cm}^2$ , 3.9  $\Omega\cdot\text{cm}^2$ , and 1.78  $\Omega\cdot\text{cm}^2$ , respectively. It was expected that the increased number of contact points of the turbuliser brush, spaced along the region of the cell where current was being produced, would lead to outperforming the single central current collector. But in effect, the MPD turbuliser caused an ohmic resistance 24% higher and a current density at 0.7 V of 43% lower than for the central nickel current collector.

In order to determine any negative impact of the turbuliser on the pressure drop along the anode, tests with and without the turbuliser were conducted as follows. The polarisation and power plots of cells with central nickel connection with additional turbuliser anode contacting in place but not electrically connected were compared to the same cell without the turbuliser. The turbuliser was carefully removed (at temperature) from the cell and extracted through the outlet manifold. The central nickel current collector was then tested again. As seen in Figure 11, the difference in performance was negligible, indicating that at these fuel conditions and operating temperatures, the turbuliser had negligible impact on the fuel flow and the electrochemical performance of the cell. This was expected given the function of the turbuliser was optimised here for current collection rather than flow enhancement. However, the result is still important in that the design did not negatively affect the performance of the cell. As discussed previously, the thermal enhancement of the turbuliser in a real system (without a furnace) will be more significant and contribute to increasing system thermal efficiency and start-up time. In a real-world stack, the turbuliser will ensure that more of the active cell length will be at the operating temperature and that thermal equilibrium is achieved. This increase in temperature of the current producing region will result in a higher electrochemical performance of the cell [5]. These effects will be further exaggerated in stacks with poor pre-heated air flow.

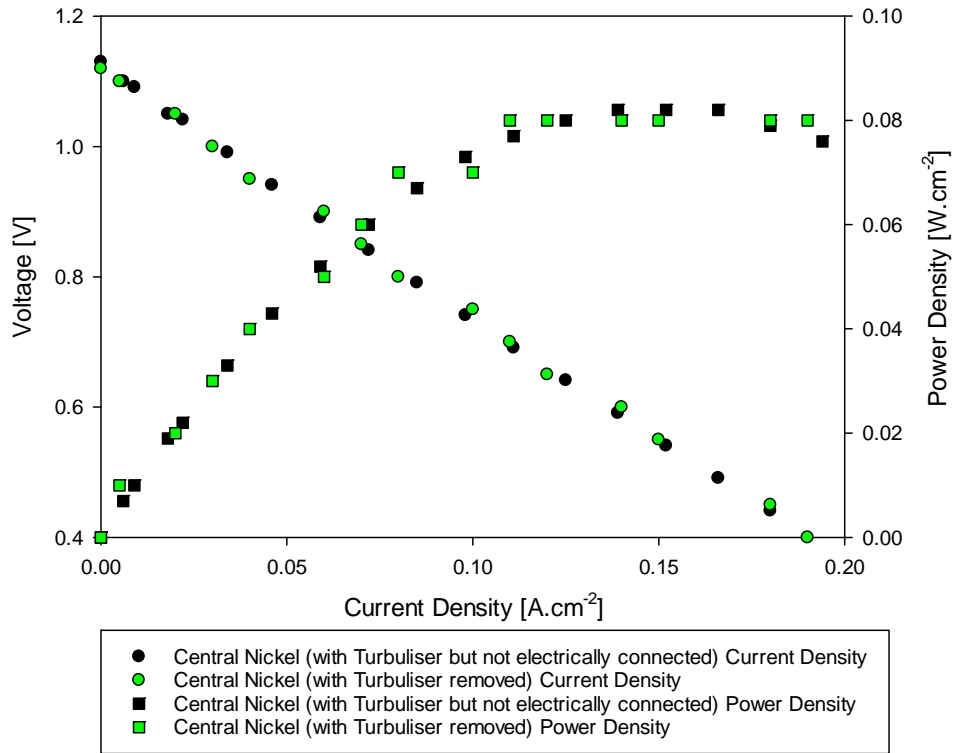


**Figure 11 - Polarisation and power density plot of a central nickel connection with turbuliser in place but not electrically connected, versus central nickel connection with the turbuliser removed.**

### 3.6 Turbuliser Materials Development and Coatings

The MPD turbuliser was then fabricated in silver to compare the effects of the material on the cell performance for comparison with the same design fabricated from nickel wire. The polarisation and power plots are seen in Figure 12 with cells operating at 750°C and 200 ml.min<sup>-1</sup> of H<sub>2</sub> and 10 ml.min<sup>-1</sup> N<sub>2</sub> flow. The current density at 0.7 V of the MPD turbuliser in nickel and silver was 0.082 A.cm<sup>-2</sup> and 0.090 A.cm<sup>-2</sup>, respectively, with the peak power density 0.057 W.cm<sup>-2</sup> and 0.096 W.cm<sup>-2</sup>, respectively. The ASR as estimated from the polarisation plot was 5.09 Ω.cm<sup>2</sup> and 3.93 Ω.cm<sup>2</sup>, respectively. The shape of the polarisation plot of the silver MPD turbuliser was atypical. Below 0.7 V the polarisation plot became flatter, suggesting a lower polarisation resistance in this region. While this change in gradient started in the ohmic polarisation region, the non-linear behaviour continued into the mass transport dominated region. The increasing temperature of the cell and wires at higher current density led to an expansion of the silver turbuliser. Given the relatively higher CTE of silver compared to the anode, the contact force between the wire and the anode apparently increased and resulted in lower contact resistance.

**Place Figure 12 here**

**Figure 12 - Polarisation and power density plots of MPD turbuliser fabricated in silver and in nickel.**

While the initial performance of the silver MPD turbuliser with respect to peak power density was superior to that of the nickel, over the first hour of testing the cell performance fluctuated and the degradation was far greater than that of the nickel specimen. This was due to the softening of the silver given the proximity of the annealing and melting temperature of silver to the SOFC operating temperature. The brush-like design of the turbuliser necessitated a mechanical spring force from the coils to maintain in contact with the anode wall. During the startup and operation of the cell, the structure of the silver turbuliser brush was compromised, resulting in a loss of contact, primarily at the upper wall surface, where sagging originated. The loss of contact points/area and contact force led to an increase in contact resistance and thus an increased ohmic polarisation of the internal current collector. This loss of contact of an internal silver current collector during operation was similar to that observed by Dhir et al. [22]. While some current could still be drawn in its compromised geometric form, the current collector could easily be dislodged if  $\mu$ T-SOFC cells were integrated into a portable device, particularly if the cell/stack was operated in a vertical orientation. In addition, the ensuing power fluctuations could damage system components if not managed properly. The data from impedance and polarisation plots of cells with the same current collection design but different materials from this study were consistent with those found in literature. The average current density at 0.7 V of tubular cells reported in academic literature at 750°C using nickel was 0.5 A.cm<sup>-2</sup> which increased by 55% to 0.77 A.cm<sup>-2</sup> when using silver. Peak power density at the same conditions was increased by 32%. The relatively higher cost and price

fluctuation of silver versus nickel, combined with the poor mechanical properties of silver outweighed its lower resistivity and therefore nickel was chosen as the primary material for further optimisation of the turbuliser internal current collector [31,32]. A plot of typical current collector material resistivity over a range of SOFC operating temperatures as well as the market price fluctuation of silver and nickel between January 2015 and January 2021 can be seen in SM Section 8.0.

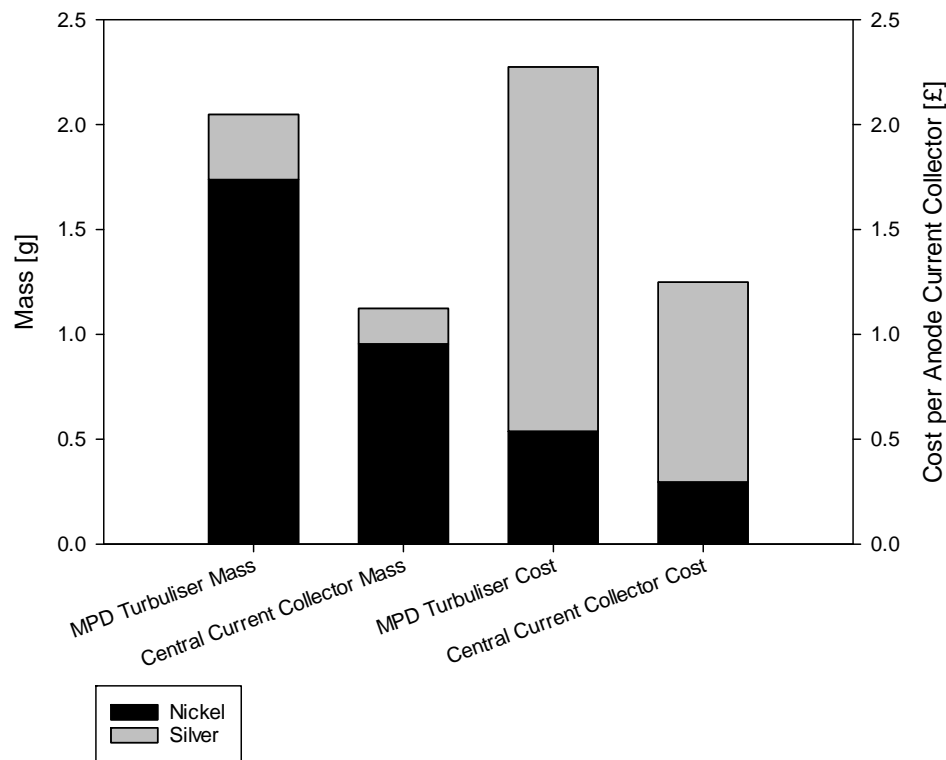


**Figure 13 - Cost and mass of the central anode current collector and MPD turbuliser made from silver versus nickel.**

In order to reduce the ohmic resistance of the nickel turbuliser current collector, the objective was to increase the bulk conductivity of the turbuliser and/or reduce the contact resistance between the turbuliser brush and the electrode. To do so, coating of the nickel turbuliser in a more conductive material was trialled. Given the success of the central silver current collector, silver was identified as the primary conductive material to be used with gold as a second candidate.

Electroplating is a low-cost option to apply coatings and can be achieved at scale in a time-effective way. The typically thin coatings of plated material had a greater impact on the contact resistance than the bulk conductivity. Two coating thicknesses were selected, 15  $\mu\text{m}$  and 30  $\mu\text{m}$  with a variance of  $\pm 5 \mu\text{m}$ . Once the coatings were applied, the coated turbulisers were heated in  $\text{N}_2$  for 1 hour at 750°C. This aimed at sintering the silver and gold particles to the support and improving the adherence in order to prevent the coatings being sheared off during the installation of the turbuliser in the cell. Electroplating was conducted at the School of Jewellery at Birmingham City

University. The plated turbulisers can be seen in SM Section 6.0. Silver nanoparticles have been used in the past to join SOFC interconnects to a Ni-YSZ anode but this technique was not explored in this study [33].

The measurement probes of a TTI BS407 Precision Milliohmmeter were clamped on the core wire just before and after the coil section. The resistance decreased by 35.8% and 58.5% for the thin and thick silver coating, respectively, compared to the standard nickel MPD design. The resistance decreased by 16.8% and 20.7% for the thin and thick gold coatings, respectively, compared to the standard nickel turbuliser. The resistance of the silver MPD turbuliser decreased by 90.4% over the nickel type. By sintering the thinly silver plated turbuliser, the resistance decreased by 5.3%, and by 7% for the thicker coating. The resistance of the silver turbuliser was one quarter of the thick silver plated specimen. The sintered thick silver coating and silver based designs were chosen for further testing. A plot of the uncoated, coated and base silver turbuliser resistances can be seen in SM Section 7.0.

The polarisation and power density plots of the thick silver plated MPD turbulisers, and the previously presented nickel and silver MPD turbulisers (for reference) are seen in Figure 14. All of the cell data presented was recorded at the standard operating conditions of 750°C with a flow of 200 ml.min<sup>-1</sup> of H<sub>2</sub> and 10 ml.min<sup>-1</sup> of N<sub>2</sub>. The current density at 0.7 V was 0.379 A.cm<sup>-2</sup> for the silver plated turbuliser with a peak power density of 0.267 W.cm<sup>-2</sup>. The ASR as estimated from the gradient of the polarisation plot was 0.83 Ω.cm<sup>2</sup>. The peak power density of the silver plated MPD turbuliser was around 4.3 times and 2.8 times higher than the nickel and silver MPD turbulisers, respectively. The ASR of the silver plated MPD turbuliser was reduced to 16% and 21% of the nickel and silver MPD values, respectively.

The relatively lower resistance of the silver turbuliser in comparison with the nickel MPD and silver plated specimen did not translate into a superior performance. This was due to the aforementioned thermomechanically induced deformation of the silver turbuliser brushes at the SOFC operating temperature. The coating of the nickel turbuliser in silver dramatically improved the performance of the current collector. The superior mechanical performance of the nickel versus silver at high temperature lent itself as current collector with superior contact and contact force. The nickel turbuliser acted well as a support for a more conductive coating material. It was clear then that the contact force, determining the contact resistance, was an important factor in current collector design. The bulk conductivity of the silver turbuliser was far higher than that of both the solid nickel and silver coated nickel ones. However, the contact resistance of the solid silver and silver coated turbulisers, given the same contact force, would be very similar.

**Place Figure 14 here**

**Figure 14 - Polarisation and power density plot of nickel hiTRAN® MPD, silver plated (nickel) hiTRAN® MPD and hiTRAN® MPD in silver at 750°C with a flow of 200 ml.min<sup>-1</sup> of H<sub>2</sub> and 10 ml.min<sup>-1</sup> N<sub>2</sub>.**

The polarisation density power plot operating on a flow of 200 ml.min<sup>-1</sup> of H<sub>2</sub> and 10 ml.min<sup>-1</sup> of N<sub>2</sub> at 750°C of the thick gold plated turbuliser was compared to that of the thick silver plated one at the same conditions as seen in Figure 15. The gold plating improved the performance of the nickel turbuliser, but not as much as the silver plating. The gold plated turbuliser achieved a current density at 0.7 V of 0.11 A.cm<sup>-2</sup> and a peak power density of 0.087 W.cm<sup>-2</sup>. The ASR of the cell as estimated from the polarisation plot was 3.23 Ω.cm<sup>-2</sup>. The peak power density of the gold plated MPD turbuliser was 45% higher than for nickel material but 33% of the value for the silver plated turbuliser. The ASR of a cell with gold plated turbuliser was 57% of that for the nickel variant and 3.9 times higher than for the silver plated specimen.

In addition to the improvement in electrochemical performance of the coated turbuliser current collectors, improved durability could be expected, given that silver and gold are more oxidation resistant than bare nickel [34]. While this is not so important for internal anode current collection in tubular cells, the inert coating will protect any wiring that will be used for interconnection to the cathode side, for example, the tail wire leaving through the laser cut slot. While silver coating has a higher electrical conductivity than the gold coating, which results in a higher performance, gold has a higher melting point than silver and is more inert. However, gold is significantly more expensive than silver [31].

**Place Figure 15 here**

**Figure 15 - Polarisation and power density plots of silver and gold plated turbuliser.**

### **3.7 Turbuliser -Anode Mechanical Testing**

While the contacting of nickel based turbuliser MPD designs was good upon installation, after heating to the SOFC operating temperature the difference in CTE between the nickel and the Ni-YSZ anode and the mechanical weakening with high temperature led to a decrease in contact force resulting in an increased contact resistance, thereby cancelling out any improvement in performance that was achieved by plating in silver or gold.

The force required to extract the turbuliser as installed and after electrochemical testing is seen in Figure 16. The peak load post-test was around 10 times lower at 7.39 N, a 90.3% decrease of the pre-test value. A load of this value meant that the turbuliser would fall out of the cell if held vertically and would certainly become dislodged if the cell/stack was being moved, which would occur if powering a portable device. The dislodging of the turbuliser could lead to short-circuiting and cause physical damage to cell and stack components. The gain in performance as a result of plating the nickel brushes would be lost over the operation of the cell, further increased by thermal cycling. The loss of contact would contribute to a substantial increase in the degradation rate of the cell. Unstable performance resulting from dodgy contacts could damage stack and system components. A solution was required to securely attach the turbuliser to the anode surface. This



would improve the properties of the turbuliser as a current collector, supplying a lower contact resistance and reducing the conductive heat transfer resistance from a heat transfer perspective.

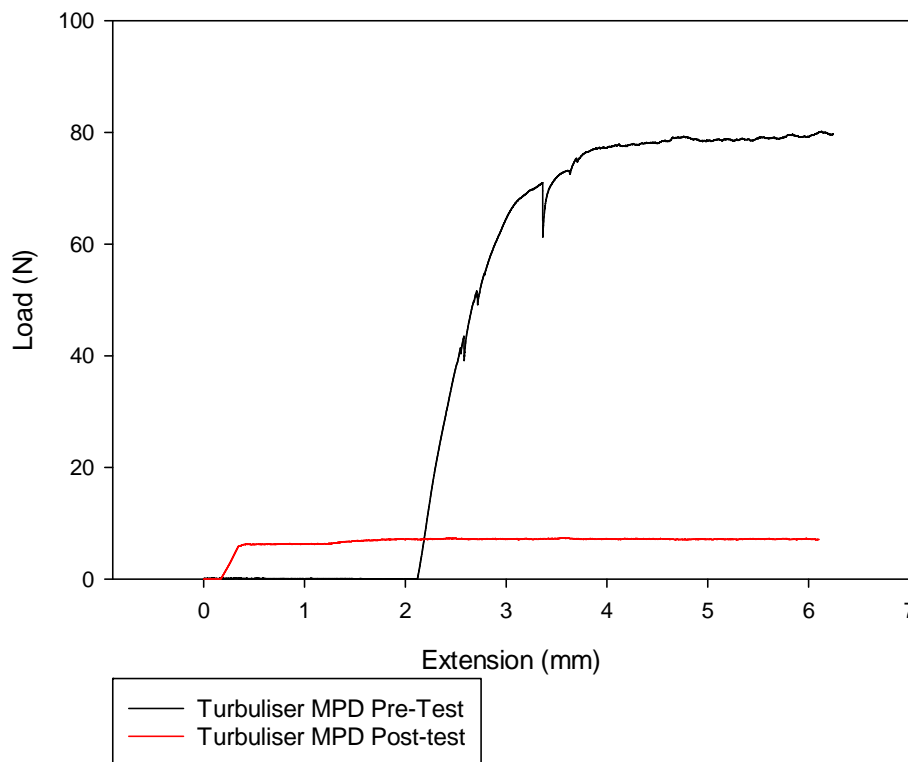


Figure 16 - Mechanical load-extension test of MPD turbuliser pre- and post-testing in a fuel cell.

## 4.0 Conclusion

A novel internal, brush-like structure called hiTRAN<sup>®</sup> used as a flow turbuliser in heat exchanger technology was adopted and adapted for use as a  $\mu$ T-SOFC current collector. Three hiTRAN<sup>®</sup> turbuliser designs were fabricated in nickel with varying loop packing density. All of the designs were characterised with respect to mass, electrical resistance and thermofluidynamic enhancement. The turbuliser modified the pressure drop and temperature profile of the  $\mu$ T-SOFC, however, the effects were dampened somewhat by the furnace and testing conditions used in this study and would be more significant and beneficial in a real-world  $\mu$ T-SOFC in improving the system thermal efficiency. Crucially the turbuliser did not negatively impact the electrochemical performance of the cell. Each design was electrochemically tested as a  $\mu$ T-SOFC current collector with the polarisation and impedance data favouring the medium packing density turbuliser. The performance of the medium package density (MPD) turbuliser as a current collector was compared with a state-of-art central current collector design, also made from nickel, for consistency. The turbuliser did not perform as well as expected given the large current collecting span of the turbuliser across the active region of the cell. From impedance analysis, it was determined that the ohmic polarisation and ASR when

using the turbuliser as a current collector was too high. To improve the performance of the turbuliser, methods to reduce the contact resistance between the turbuliser brushes and the anode were explored. The MPD type was fabricated in silver with the objective of increasing the bulk conductivity and decreasing the contact resistance. However, at the operating temperature, the relatively poor mechanical integrity of silver (w.r.t nickel) and structural requirements of the brush-like turbuliser design led to a loss of contact of the internal current collector with the anode and an increased contact resistance. The performance was not as high as expected and the design would not be suitable for even short term operation of a stationary or portable device. Coating of the nickel turbuliser with highly conductive precious metals was then explored to reduce the -anode contact resistance. Gold and silver were trialled at two different thicknesses with the thicker silver coating being the best performer. The final design thick silver plated MPD turbuliser design achieved a current density at 0.7 V of  $0.38 \text{ A.cm}^{-2}$  and peak power density of  $0.27 \text{ W.cm}^{-2}$ , 4.3 times higher than the original non-plated design and 3.3 times higher than the state-of-the-art central nickel current collector.

However, separation of the nickel turbuliser due to thermal mismatch with the fuel cell led to separation of the spring fitted turbuliser during steady-state operation which was further exasperated by thermal cycling. It was therefore concluded that a technique would be required to form a physically strong joint between the turbuliser and anode.

## Acknowledgement

This work was supported by the Centre for Doctoral Training (CDT) in Fuel Cells and their Fuels, which is part-funded by the EPSRC under contract EP/L015749/1. Acknowledgements go to CALGAVIN Ltd for supplying hiTRAN® turbulisers and the associated resources for production.

## References

- [1] R. O'Hayre, S.-W. Cha, W. Celella, F.B. Prinz, Fuel Cell Fundamentals, Second, John Wiley & Sons, New York, USA, 2009.
- [2] W. Bujalski, C.M. Dikwal, K. Kendall, Cycling of three solid oxide fuel cell types, J. Power Sources. 171 (2007) 96–100.doi:10.1016/j.jpowsour.2007.01.029.
- [3] K. Kendall, Introduction to SOFCs, in: High-Temperature Solid Oxide Fuel Cells 21st Century, Elsevier, London, England, 2016: pp. 1–24.
- [4] K. Kendall, M. Kendall, K. Kendall, Portable early market SOFCs, in: High-Temperature Solid Oxide Fuel Cells 21st Century, Elsevier, London, England, 2016: pp. 329–356.
- [5] J. Larminie, A. Dicks, Fuel Cell Systems Explained, John Wiley & Sons, Chichester, England, 2006.
- [6] R. De La Torre, H.J. Avila-Paredes, V.M. Sglavo, Comparative performance analysis of anode-supported micro-tubular SOFCs with different current-collection architectures, Fuel Cells. 13

- (2013) 729–732.doi:10.1002/face.201300010.
- [7] D. Cui, B. Tu, M. Cheng, Effects of cell geometries on performance of tubular solid oxide fuel cell, *J. Power Sources*. 297 (2015) 419–426.doi:10.1016/j.jpowsour.2015.08.013.
  - [8] Y. Bai, C. Wang, C. Jin, J. Liu, Anode Current Collecting Efficiency of Tubular Anode-supported Solid Oxide Fuel Cells, *Fuel Cells*. 11 (2011) 465–468.doi:10.1002/face.201000053.
  - [9] O. Hodjati-Pugh, A. Dhir, R. Steinberger-Wilckens, Internal Current Collection in Microtubular SOFCs : Minimisation of Contact Resistance via Brazing and Plating, *ECS Trans*. 91 (2019) 553–548.doi:doi.org/10.1149/09101.0533ecst.
  - [10] A. Meadowcroft, K. Howe, A. Dhir, R. Steinberger-Wilckens, Connection Optimisation for Micro-Tubular Solid Oxide Fuel Cells (A1507), in: 11th Eur. SOFC SOE Forum, Lucerne Switzerland, 2014.
  - [11] A. Dhir, Improved microtubular solid oxide fuel cells. Doctoral Thesis, University of Birmingham, 2008.
  - [12] P.A. Lessing, A review of sealing technologies applicable to solid oxide electrolysis cells, *J Mater Sci*. (2007) 3465–3476.doi:10.1007/s10853-006-0409-9.
  - [13] A.G. Sabato, G. Cempura, D. Montinaro, A. Chrysanthou, M. Salvo, E. Bernardo, M. Secco, F. Smeacetto, Glass-ceramic sealant for solid oxide fuel cells application: Characterization and performance in dual atmosphere, *J. Power Sources*. 328 (2016) 262–270.doi:10.1016/j.jpowsour.2016.08.010.
  - [14] K. Kendall, M. Kendall, N.Q. Minh, Cell and stack design, fabrication and performance, in: *High-Temperature Solid Oxide Fuel Cells 21st Century*, Elsevier, London, England, 2016: pp. 255–282.
  - [15] K.S.Ä. Weil, B.J. Koeppel, Thermal stress analysis of the planar SOFC bonded compliant seal design, *Int. J. Hydrogen Energy*. 33 (2008) 3976–3990.doi:10.1016/j.ijhydene.2007.11.008.
  - [16] K. Kendall, M. Slinn, J. Preece, Formulating liquid ethers for microtubular SOFCs, *J. Power Sources*. 157 (2006) 750–753.doi:10.1016/j.jpowsour.2006.01.061.
  - [17] C. Liu, J. Pu, X. Chen, Z. Ma, X. Ding, J. Zhou, S. Wang, Influence of anode’s microstructure on electrochemical performance of solid oxide direct carbon fuel cells, *Int. J. Hydrogen Energy*. 45 (2020) 11784–11790.doi:10.1016/j.ijhydene.2020.02.119.
  - [18] W. Huang, C. Finnerty, R. Sharp, K. Wang, B. Balili, High-Performance 3D Printed Microtubular Solid Oxide Fuel Cells, *Adv. Mater. Technol*. 2 (2017) 1–5.doi:10.1002/admt.201600258.
  - [19] O. Hodjati-Pugh, A. Dhir, R. Steinberger-Wilckens, The development of current collection in micro-tubular solid oxide fuel cells—a review, *Appl. Sci*. 11 (2021) 1–27.doi:10.3390/app11031077.
  - [20] S.-B. Lee, T.-H. Lim, R.-H. Song, D.-R. Shin, S.-K. Dong, Development of a 700 W anode-supported micro-tubular SOFC stack for APU applications, *Int. J. Hydrogen Energy*. (2008).doi:10.1016/j.ijhydene.2008.02.034.
  - [21] V. Lawlor, S. Griesser, G. Buchinger, A.G. Olabi, S. Cordiner, D. Meissner, Review of the micro-tubular solid oxide fuel cell Part I . Stack design issues and research activities, *J. Power Sources*. 193 (2009) 387–399.doi:10.1016/j.jpowsour.2009.02.085.
  - [22] A. Dhir, K. Kendall, Improving Reliability of Microtubular SOFCs for Direct Use on Methane, *ECS Tran*. 7 (2007) 823–828.doi:10.1149/1.2729171.
  - [23] V. Lawlor, Review of the micro-tubular solid oxide fuel cell (Part II : Cell design issues and research activities), *J. Power Sources*. 240 (2013) 421–441.doi:10.1016/j.jpowsour.2013.03.191.
  - [24] S. Naga Sarada, K.K. Radha, A.V.S. Raju, Experimental investigations in a circular tube to enhance turbulent heat transfer using mesh inserts, *J. Eng. Appl. Sci*. 4 (2009) 53–60.
  - [25] M. Rahimi, B. Aghel, A.A. Alsairafi, Chemical Engineering and Processing : Process Intensification Experimental and CFD studies on using coil wire insert in a proton exchange membrane fuel cell, *Chem. Eng. Process. Process Intensif*. 49 (2010) 688–695.doi:10.1016/j.cep.2009.11.003.

- [26] J. Murray, Pressure loss and heat transfer for single-phase turbulent flow in tubes fitted with wire-matrix inserts. Doctoral Thesis, University of Birmingham, 2009.
- [27] G.O. Brown, The History of the Darcy-Weisbach Equation for Pipe Flow Resistance, *Environ. Water Resour. Hist.* (2003) 34–43.doi:10.1061/40650(2003)4.
- [28] R.B. Bird, W. Stewart, E. Lightfoot, *Transport Phenomena*, Second Edi, Wiley, Vicksburg, USA, 2007.
- [29] P. Drogemuller, The Use of hiTRAN Wire Matrix Elements to Improve the Thermal Efficiency of Tubular Heat Exchangers in Single and Two-Phase Flow, *Chem. Ing. Tech.* 81 (2015) 188–202.doi:10.1002/cite.201400081.
- [30] A. Meadowcroft, S.R. Howroyd, K. Kendall, M. Kendall, Testing microtubular SOFCs in unmanned air vehicles (UAVs), *ECS Trans.* 57 (2013) 451–457.doi:10.1149/05701.0451ecst.
- [31] Daily Metal Prices, (2020). <https://www.dailymetalprice.com/metalpricecharts.php?c=cu&u=lb&d=20> (accessed August 1, 2020).
- [32] J.W. Fergus, Metallic interconnects for solid oxide fuel cells, *Mater. Sci. Eng. A.* 397 (2005) 271–283.doi:10.1016/j.msea.2005.02.047.
- [33] X. Si, J. Cao, S. Liu, X. Song, J. Qi, Y. Huang, J. Feng, Fabrication of 3D Ni nanosheet array on Crofer22APU interconnect and NiO-YSZ anode support to sinter with small-size Ag nanoparticles for low-temperature sealing SOFCs, *Int. J. Hydrogen Energy.* 43 (2018) 2977–2989.doi:10.1016/j.ijhydene.2017.12.132.
- [34] K. Kendall, M. Kendall, L. Niewolak, F. Tietz, W.J. Quadackers, Interconnects, in: *High-Temperature Solid Oxide Fuel Cells 21st Century*, Elsevier, London, England, 2016: pp. 195–254.